

Fractional phase measurement of BDS-3 B1C signals via simulated carrier phase observation of Rydberg atom antenna

Guanyu Ren(任冠宇), Zheng Yin(尹政), Wenning Gao(高文宁), Zhifeng Han(韩志凤), Zhengmao Jia(贾政茂), Jun Qian(钱军), Qingan Ding(丁庆安), Yandong Peng(彭延东)

Citation: Chin. Phys. B.2026. 35(**8**): 084202. DOI: 10.1088/1674-1056/ae6ccc
http://cpb.iphy.ac.cn; http://iopscience.iop.org/cpb

What follows is a list of articles you may be interested in

Generation of squeezed states of magnons and photons based on the Kerr effect in cavity-magnon hybrid system

Cheng-Hua Bai(白成华) and Suying Bai(白素英)
Chin. Phys. B, 2026, 35 (**4**): 044210. DOI: 10.1088/1674-1056/ae4b2d

Role of trajectory symmetry in solid high-order harmonic generation

Shuang Wang(王爽), Yu Zhao(赵宇), Hui-Rong Wang(王慧荣), Yun-He Xing(邢云鹤), Xiao-Xin Huo(霍晓鑫), and Jun Zhang(张军)
Chin. Phys. B, 2026, 35 (**4**): 044204. DOI: 10.1088/1674-1056/ae04da

Decoherence and evolution of a general quadratic state for amplitude decay

Zhi-Long Wan(万志龙), Hong-Chun Yuan(袁洪春), Xiao-Lei Yin(尹晓蕾), and Chang-Ying Wang(王昌英)
Chin. Phys. B, 2026, 35 (**2**): 024204. DOI: 10.1088/1674-1056/adeb5f

Phase sensitivity of a lossy truncated SU(1,1) interferometer with double-port homodyne detection

Yu-Wei Xiao(肖煜伟), Yue Ji(吉悦), Jia-Yi Wei(魏嘉怡), Jian-Dong Zhang(张建东), and Li-Li Hou(侯丽丽)
Chin. Phys. B, 2026, 35 (**1**): 014205. DOI: 10.1088/1674-1056/adfd46

An ultrafast and low-power slow light tuning mechanism for compact aperture-coupled disk resonators

Bo-Yun Wang(王波云), Yue-Hong Zhu(朱月红), Jing Zhang(张静), Qing-Dong Zeng(曾庆栋), Jun Du(杜君), Tao Wang(王涛), Hua-Qing Yu(余华清)
Chin. Phys. B, 2020, 29 (**8**): 084211. DOI: 10.1088/1674-1056/ab9df1

SPECIAL TOPIC — Quantum frontiers with Rydberg atoms

Fractional phase measurement of BDS-3 B1C signals via simulated carrier phase observation of Rydberg atom antenna

Guanyu Ren(任冠宇)[1], Zheng Yin(尹政)[1], Wenning Gao(高文宁)[2], Zhifeng Han(韩志凤)[1], Zhengmao Jia(贾政茂)[1], Jun Qian(钱军)[3], Qingan Ding(丁庆安)[1], and Yandong Peng(彭延东)[1,†]

[1] *Qingdao Key Laboratory of Terahertz Technology, College of Electronic and Information Engineering, Shandong University of Science and Technology, Qingdao* 266590, *China*
[2] *China Satellite Network Group Co., Ltd., Beijing* 100160, *China*
[3] *Hangzhou Hanggao Ruiguang Technology Co., Ltd., Hangzhou* 311101, *China*

(Received 6 March 2026; revised manuscript received 6 May 2026; accepted manuscript online 13 May 2026)

We propose a five-level atomic scheme incorporating an auxiliary microwave dressing field to achieve sensitivity at the frequency of the BeiDou Navigation Satellite System Phase 3 B1C (BDS-3 B1C) signal, specifically 1.57542 GHz. Carrier phase observation in this frequency band is simulated using the atomic homodyne technique. The contrast ratio and measurement uncertainty of the fractional phase are analyzed, together with the influence of the BDS-3 B1C signal on carrier phase observation. The simulation results show that the fractional phase measurement uncertainty is at the basic sub-radian level for E_{B1C} ranging from 0.048 V/m to 0.1 V/m, and reaches the high-precision sub-radian level for E_{B1C} in the range of 0.11 V/m to 0.25 V/m. The distance measurement error coefficient is 0.0014 V, with a minimum measurement error of 0.82 cm. In addition, the influence of half-cycle slips on the uncertainty of fractional phase measurements is analyzed.

Keywords: carrier phase observation, BDS-3 B1C signals, Rydberg atom antenna

PACS: 42.50.Dv, 42.50.Gy

DOI: 10.1088/1674-1056/ae6ccc **CSTR:** 32038.14.CPB.ae6ccc

1. Introduction

Carrier phase observation, characterized by its high precision and phase sensitivity, is the core technology for achieving high-precision positioning in satellite navigation. It is known that this type of observation is susceptible to the influence of multiple error sources, among which half-cycle slip[1–3] is one of the key factors restricting its measurement resolution. Reducing pseudorange[4] measurement errors and improving the measurement resolution of carrier phase remain challenging. In the reception and processing of carrier signals, achieving these objectives hinges on the precise measurement of microwave fields. Quantum technology based on Rydberg atoms has attracted significant attention in the field of microwave metrology,[5–9] and is now extending to communications.[10–12]

Most of these applications are based on radio frequency (RF) sensing, which utilizes electromagnetically induced transparency (EIT) or Autler–Townes (AT)[13–15] splitting effects in Rydberg atoms to achieve pronounced advantages over conventional sensors. First, highly excited Rydberg atoms have a large electric dipole moment and exhibit high sensitivity to external electric fields, enabling the detection of weak RF fields with a sensitivity on the order of $\mu\mathrm{V}\cdot\mathrm{m}^{-1}\cdot\mathrm{Hz}^{-1/2}$.[16,17] Secondly, dense jump channels between highly excited states enable coverage from MHz to THz[18–22] frequency bands through laser tuning, free from the constraints of conventional antenna structures. Thirdly, the atomic self-calibration property[13,23] achieves absolute measurement of RF field frequency and amplitude without external calibration. Rydberg atom antennas overcome the Chu limit[24,25] for traditional electronic sensors, which relates Q-factor limitations to physical size. Finally, by leveraging quantum state evolution, Rydberg atoms can directly demodulate baseband signals from carrier frequencies, bypassing conventional demodulation circuits and offering a novel approach to communication technologies.[26–30]

For interferometric phase sensing, many approaches are based on Rydberg atom antennas. These include heterodyne[27] and super-heterodyne,[16,17,31] closed-loop schemes,[7,32,33] the Floquet EIT technique,[34,35] and all-optical phase detectors,[36] among others. These approaches are subject to some limitations in the carrier phase observation of BDS-3 B1C signals. Most schemes operate in the super-high frequency (SHF, 3–30 GHz) band, where sufficient sensitivity can be achieved without resorting to high-angular-momentum Rydberg states or elevated principal quantum numbers. Conventional EIT configurations, particularly those exploiting low-angular-momentum Rydberg states ($L < 3$), necessitate the use of high principal quantum numbers

†Corresponding author. E-mail: pengyd@sdust.edu.cn

© 2026 Chinese Physical Society and IOP Publishing Ltd. All rights, including for text and data mining, AI training, and similar technologies, are reserved.

($n > 90$) to access transition frequencies below 2.5 GHz in an ^{85}Rb vapor cell.[12,37] In addition, Rydberg atom antennas with principal quantum numbers $n \geq 80$ are seldom used as sensors. This is because exciting such transitions demands large amounts of laser power, causing inhomogeneous broadening via optical light shifts.[38] Concurrently, these high-n states suffer from collisional broadening driven by their increased Rydberg–Rydberg interaction cross sections.[38] Recently, utilizing multi-photon excitation to access higher angular momentum states ($L = 3$) has emerged as an effective alternative for resolving these issues in low-GHz sensing.[39,40]

In this work, we propose an efficient scheme for carrier phase observation of the BDS-3 B1C signal using Rydberg rubidium-85 atoms to measure its fractional phase. The carrier frequency of the BDS-3 B1C signal is 1.57542 GHz. In our approach, an auxiliary microwave dressing field is introduced. By increasing the angular momentum quantum number L, resonant access to the middle of the UHF band is achieved at 1.62 GHz using a Rydberg state with the principal quantum number $n = 37$. This relatively low value of n minimizes detuning with respect to the BDS-3 B1C signal and avoids the inhomogeneous broadening and collisional broadening effects inherently brought by high-n states. Under homodyne[26] conditions, the frequency lock between the LO and BDS-3 B1C signal fields makes the interference signal intensity depend on their relative phase difference,[41] which enables the detection of minute phase variations. Our analysis further shows that a half-cycle slip induces an abrupt π-radian phase shift and degrades both the contrast ratio and the resolution of the fractional phase, consequently impairing the stability of carrier phase observation. Thus, our research on half-cycle slips helps improve the robustness and resolution of Rydberg atom antennas.

2. Model and basic equations

The model of a five-level ^{85}Rb Rydberg atom is considered as shown in Fig. 1(a). A probe field (795 nm) and a control field (482 nm) drive the ground-state transition $|1\rangle \rightarrow |2\rangle$ (D1 line),[42] and the excited-state transition $|2\rangle \rightarrow |3\rangle$, respectively. An auxiliary microwave dressing field with Rabi frequency $\Omega_{\rm d}$ drives the $|3\rangle \rightarrow |4\rangle$ transition at a resonant frequency of 182.96 GHz. Two adjacent Rydberg states $37F_{5/2}$ and $37G_{7/2}$ are coupled via a strong LO field ($\Omega_{\rm L}$) at 1.62 GHz, corresponding to the $|4\rangle \rightarrow |5\rangle$ transition. These resonant frequencies are calculated using the Alkali Rydberg Calculator (ARC).[43] A schematic diagram is illustrated in Fig. 1(b). The counter-propagating configuration (probe field and control field) effectively suppresses the optical Doppler effect. Because the residual Doppler broadening merely attenuates the macroscopic signal amplitude without altering the velocity-independent microwave homodyne interference, we focus our analysis on the central velocity group ($v = 0$) to clearly demonstrate the underlying phase measurement mechanism. The microwave dressing field is produced by a horn collinear with the probe beam, and the B1C and LO fields are provided by a waveguide behind the cell.[12]

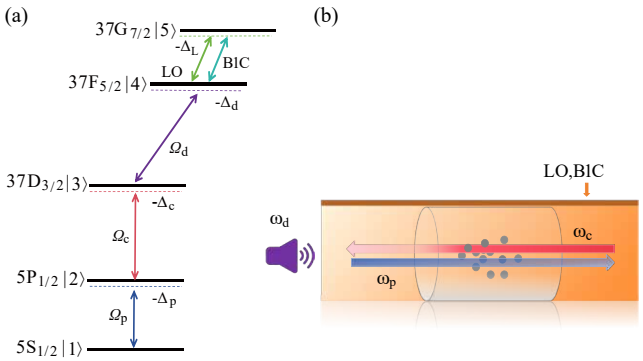


Fig. 1. (a) Five-level Rydberg atomic model. (b) Schematic diagram of the coupling with atoms.

In the interaction picture and after the rotating wave approximation (RWA), the Hamiltonian of the system can be written as

$$\boldsymbol{H} = \frac{1}{2}\hbar \begin{pmatrix} 0 & \Omega_{\rm p} & 0 & 0 & 0 \\ \Omega_{\rm p} & -2\Delta_{\rm p} & \Omega_{\rm c} & 0 & 0 \\ 0 & \Omega_{\rm c} & -2(\Delta_{\rm c}+\Delta_{\rm p}) & \Omega_{\rm d} & 0 \\ 0 & 0 & \Omega_{\rm d} & -2(\Delta_{\rm c}+\Delta_{\rm p}+\Delta_{\rm d}) & \Omega_{\rm L} \\ 0 & 0 & 0 & \Omega_{\rm L} & -2(\Delta_{\rm c}+\Delta_{\rm p}+\Delta_{\rm d}+\Delta_{\rm L}) \end{pmatrix}, \tag{1}$$

where $\Delta_m = \omega_m - \omega_{\rm atom}$ ($m = {\rm p,c,d,L}$) denotes the frequency detuning of the corresponding field, and $\omega_{\rm atom}$ represents the resonant transition frequency between the two atomic energy levels coupled by field m. In the context of carrier phase observations, the modulation of the BDS-3 B1C signal can be approximated as Binary Phase Shift Keying (BPSK). Consequently, the B1C signal field can be expressed as $E_{\rm B1C}\cos(\omega_{\rm B1C}t + \varphi_{\rm B1C})$. The LO field is used to detect the BDS-3 B1C signal, and its frequency is set equal to that of the BDS-3 B1C signal to perform carrier phase observation. The atomic homodyne technique is employed to ensure frequency identity, with $\omega_{\rm B1C} = \omega_{\rm LO}$ and $E_{\rm B1C} \ll E_{\rm LO}$. The total electric field ($E_{\rm tot}$) received by Rydberg atoms consists of both the LO and B1C fields, i.e., $E_{\rm LO}\cos(\omega_{\rm LO}t + \varphi_{\rm LO})$ and $E_{\rm B1C}\cos(\omega_{\rm B1C}t + \varphi_{\rm B1C})$. The phase difference between the B1C and LO fields is $\Delta\varphi = \varphi_{\rm B1C} - \varphi_{\rm LO}$, which corre-

sponds to the carrier phase observable. It can be expressed as $\Delta\varphi = N\cdot 2\pi + \delta\phi$, where N is the integer ambiguity (full-cycle portion) and $\delta\phi \in [0, 2\pi)$ is the fractional phase. Due to the integer ambiguity problem in long-baseline satellite positioning, which is typically resolved using differential techniques or precise orbit determination, this work focuses exclusively on optimizing the measurement resolution of $\delta\phi$. Based on $\omega_{\mathrm{B1C}} = \omega_{\mathrm{LO}}$, the LO field detuning Δ_{L} is 44.58 MHz. Therefore, in the off-resonant region, the probe transmission T is related to the square of E_{tot} and is given by[26,44]

$$T \propto \left\langle E_{\mathrm{tot}}^2 \right\rangle \approx \frac{E_{\mathrm{LO}}^2}{2} + \frac{E_{\mathrm{B1C}}^2}{2} + E_{\mathrm{LO}} E_{\mathrm{B1C}} \cos(\Delta\varphi). \tag{2}$$

The time evolution of the system's density matrix ρ is governed by the Liouville–von Neumann equation, incorporating the Lindblad dissipative term $\mathcal{L}(\rho)$

$$\dot{\rho} = \frac{\partial\rho}{\partial t} = -\frac{\mathrm{i}}{\hbar}[H,\rho] + \mathcal{L}(\rho), \tag{3}$$

where $\mathcal{L}(\rho)$ accounts for the dephasing processes

$$\mathcal{L}(\rho) = \begin{pmatrix} \Gamma_2\rho_{22} & -\gamma_{12}\rho_{12} & -\gamma_{13}\rho_{13} & -\gamma_{14}\rho_{14} & -\gamma_{15}\rho_{15} \\ -\gamma_{21}\rho_{21} & -\Gamma_2\rho_{22}+\Gamma_3\rho_{33} & -\gamma_{23}\rho_{23} & -\gamma_{24}\rho_{24} & -\gamma_{25}\rho_{25} \\ -\gamma_{31}\rho_{31} & -\gamma_{32}\rho_{32} & -\Gamma_3\rho_{33}+\Gamma_4\rho_{44} & -\gamma_{34}\rho_{34} & -\gamma_{35}\rho_{35} \\ -\gamma_{41}\rho_{41} & -\gamma_{42}\rho_{42} & -\gamma_{43}\rho_{43} & -\Gamma_4\rho_{44}+\Gamma_5\rho_{55} & -\gamma_{45}\rho_{45} \\ -\gamma_{51}\rho_{51} & -\gamma_{52}\rho_{52} & -\gamma_{53}\rho_{53} & -\gamma_{54}\rho_{54} & -\Gamma_5\rho_{55} \end{pmatrix}. \tag{4}$$

The decay rate $\Gamma_j = \sum_k \Gamma_{jk}$ $(j,k = 1,2,3,4,5)$ and $\gamma_{jk} = (\Gamma_j + \Gamma_k)/2$, where Γ_{jk} is the spontaneous decay rate from state $|j\rangle$ to state $|k\rangle$. Therefore, the time evolution of the density matrix elements is given as follows:

$$\begin{aligned}
\dot{\rho}_{21} &= -\gamma_{21}\rho_{21} - \mathrm{i}\left(-\Delta_{\mathrm{p}}\rho_{21} + \frac{\rho_{31}\Omega_{\mathrm{c}}}{2} + \frac{\rho_{11}\Omega_{\mathrm{p}}}{2} - \frac{\rho_{22}\Omega_{\mathrm{p}}}{2}\right), \\
\dot{\rho}_{31} &= -\gamma_{31}\rho_{31} - \mathrm{i}\left[(-\Delta_{\mathrm{c}} - \Delta_{\mathrm{p}})\rho_{31} + \frac{\rho_{21}\Omega_{\mathrm{c}}}{2}\right. \\
&\quad \left. + \frac{\rho_{41}\Omega_{\mathrm{d}}}{2} - \frac{\rho_{32}\Omega_{\mathrm{p}}}{2}\right], \\
\dot{\rho}_{41} &= -\gamma_{41}\rho_{41} - \mathrm{i}\left[(-\Delta_{\mathrm{c}} - \Delta_{\mathrm{d}} - \Delta_{\mathrm{p}})\rho_{41}\right. \\
&\quad \left. + \frac{\rho_{31}\Omega_{\mathrm{d}}}{2} + \frac{\rho_{51}\Omega_{\mathrm{L}}}{2} - \frac{\rho_{42}\Omega_{\mathrm{p}}}{2}\right], \\
\dot{\rho}_{51} &= -\gamma_{51}\rho_{51} - \mathrm{i}\left[\frac{\rho_{41}\Omega_{\mathrm{L}}}{2} - \frac{\rho_{52}\Omega_{\mathrm{p}}}{2}\right. \\
&\quad \left. + \rho_{51}(-\Delta_{\mathrm{c}} - \Delta_{\mathrm{d}} - \Delta_{\mathrm{p}} - \Delta_{\mathrm{L}})\right],
\end{aligned} \tag{5}$$

where the closed system satisfies $\sum_{n=1}^{5}\rho_{nn} = 1$, with the initial conditions $\rho_{11}^{(0)} = 1$ and $\rho_{22}^{(0)} = \rho_{33}^{(0)} = \rho_{44}^{(0)} = \rho_{55}^{(0)} = 0$. Considering the weak probe field approximation, the coherent term ρ_{21} is expressed as

$$\begin{aligned}
\rho_{21} &= -2\mathrm{i}\left[F\cdot\Omega_{\mathrm{d}}^2 + A(4B\cdot F + \Omega_{\mathrm{L}}^2)\right]\Omega_{\mathrm{p}} \\
&\quad \times\left[-4B\cdot F\cdot\Omega_{\mathrm{c}}^2 + 4F\gamma_{21}\Omega_{\mathrm{d}}^2 - 4iF\Delta_{\mathrm{p}}\Omega_{\mathrm{d}}^2\right. \\
&\quad \left. -\Omega_{\mathrm{c}}^2\Omega_{\mathrm{L}}^2 + 4A(\gamma_{21} - \mathrm{i}\Delta_{\mathrm{p}})(4B\cdot F + \Omega_{\mathrm{L}}^2)\right]^{-1}, \\
A &= -\gamma_{31} - \mathrm{i}(-\Delta_{\mathrm{c}} - \Delta_{\mathrm{p}}), \\
B &= -\gamma_{41} - \mathrm{i}(-\Delta_{\mathrm{c}} - \Delta_{\mathrm{p}} - \Delta_{\mathrm{d}}), \\
F &= -\gamma_{51} - \mathrm{i}\left(-\Delta_{\mathrm{c}} - \Delta_{\mathrm{d}} - \Delta_{\mathrm{p}} - \Delta_{\mathrm{L}}\right).
\end{aligned} \tag{6}$$

The transmission of the probe beam is given by $T = \exp(-2\pi l\,\mathrm{Im}(\chi)/\lambda_{\mathrm{p}})$, where l is the atomic vapor length and λ_{p} is the probe field wavelength. The susceptibility $\chi = N|\mu_{21}|^2\rho_{21}/(\hbar\varepsilon_0\Omega_{\mathrm{p}})$, where ε_0 is the permittivity of the vacuum, N is the atomic density, and $\hbar$ is the reduced Planck's constant.

3. Results and discussion

First, we briefly introduce the EIT spectrum and its changes driven by the dressing and LO fields as shown in Fig. 2(a). For simplicity, all parameters are scaled by the decay rate Γ ($\Gamma = \gamma_{21} = 2\pi\times 5.75$ MHz)[42] in the following discussion. Without the dressing and LO fields, the three-level Rydberg atomic system ($\Omega_{\mathrm{p}} + \Omega_{\mathrm{c}}$) exhibits a common EIT profile with a single central transmission peak of linewidth $\sim 2.5\,\Gamma$. When the microwave dressing field is applied ($\Omega_{\mathrm{p}} + \Omega_{\mathrm{c}} + \Omega_{\mathrm{d}}$), the central peak (red dashed line) splits into two peaks (blue dashed line) with a narrow linewidth of $\sim 1.3\,\Gamma$. This is induced by quantum interference between two transition paths caused by the dressing field, which enhances the sensitivity of the Rydberg atom antenna. Furthermore, when the LO field is applied ($\Omega_{\mathrm{p}} + \Omega_{\mathrm{c}} + \Omega_{\mathrm{d}} + \Omega_{\mathrm{LO}}$), the resonant absorption is suppressed, yielding a three-peak spectrum.

Upon introducing the B1C field, the atomic homodyne technique is employed to extract the carrier phase observation $\Delta\varphi$. Operating at the identical frequency, the LO and B1C fields superpose to yield a homodyne interference signal, which maps the phase difference onto the transmitted intensity I of the probe beam. Based on Eq. (2), the transmitted intensity I shown in Fig. 2(b) is expressed as

$$\begin{aligned}
I(\Delta\varphi) &= I_0 - B\cos(\Delta\varphi), \\
I_0 &= \frac{I_{\max} + I_{\min}}{2}, \quad B = \frac{I_{\max} - I_{\min}}{2},
\end{aligned} \tag{7}$$

where I_0 is the average intensity and B is the modulation amplitude. $I_{\max}$ and $I_{\min}$ are the maximum and minimum values of the intensity over the period 0 to 2π, respectively.

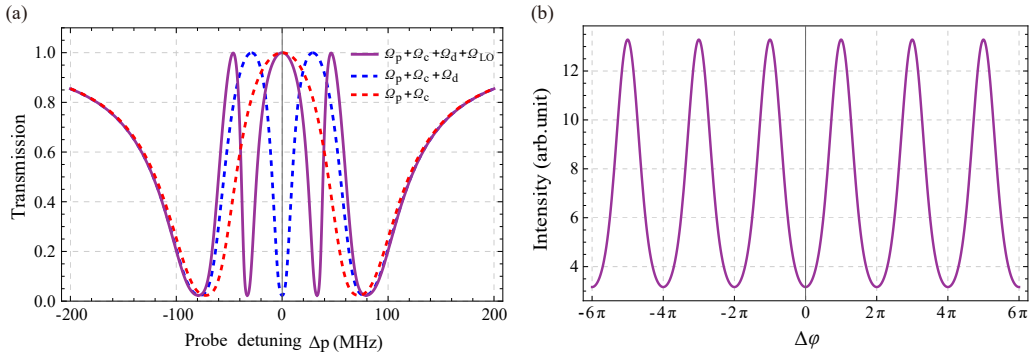


Fig. 2. (a) EIT transmission spectra with various coupling fields. $\Delta_p = \Delta_c = \Delta_d = 0$, $\Delta_L = 0$, $\Omega_p = 0.01\,\Gamma$, $\Omega_c = 4\,\Gamma$, $\Omega_L = 2\,\Gamma$, $\Omega_d = 1.6\,\Gamma$, $l = 5$ cm, $N \sim 10^9$ cm^{-3}. (b) Relationship between the carrier phase observation $\Delta\varphi$ and the transmitted intensity I. $I_0 = 8.15$, $B = 4.98$, $E_{B1C} = 0.2$ V/m, $E_{LO} = 2$ V/m, $\Delta_L = 44.58$ MHz. Other parameters are the same as those in Fig. 2(a).

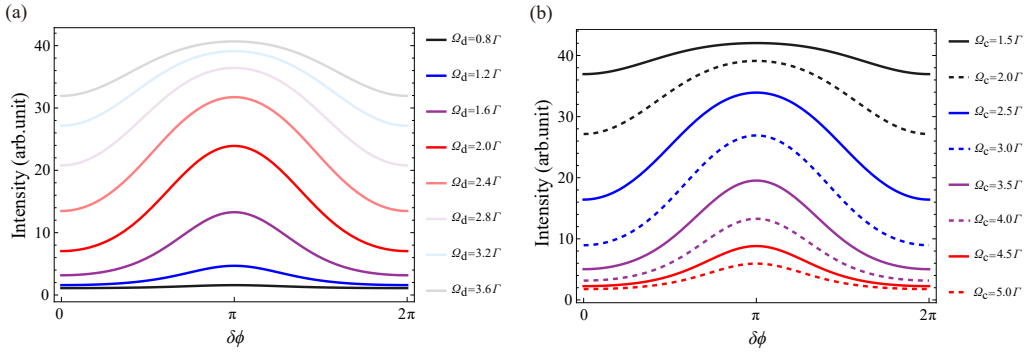


Fig. 3. (a) Variation of the transmitted intensity with $\delta\phi$ (Ω_d from 0.8 Γ to 3.6 Γ, $\Omega_c = 4\,\Gamma$). (b) Variation of the transmitted intensity with $\delta\phi$ (Ω_c from 1.5 Γ to 5.0 Γ, $\Omega_d = 1.6\,\Gamma$). Other parameters are the same as those in Fig. 2.

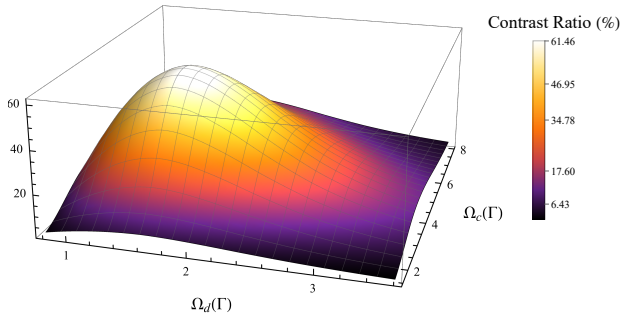


Fig. 4. Contrast ratio as a function of Ω_d and Ω_c. Other parameters are the same as those in Fig. 2.

Contrast ratio is an important indicator for evaluating phase interferometric visibility. In this work, it is defined as

$$C = \frac{I_{max} - I_{min}}{I_{max} + I_{min}}. \tag{8}$$

A higher contrast ratio C indicates a stronger modulation of transmitted intensity I by the phase difference $\Delta\varphi$, which leads to a reduction in the uncertainty of $\delta\phi$. Figures 3 and 4 show the effects of the control field Ω_c and the dressing field Ω_d on the contrast ratio C of the fractional phase $\delta\phi$ in the transmitted intensity profile. As shown in Fig. 3(a), the transmitted intensity varies with $\delta\phi$ for different Ω_d. At $\Omega_d = 0.8\,\Gamma$, the intensity response is smooth and weakly modulated, yielding a low contrast ratio of $C = 17.60\%$. As Ω_d increases, C rises due to enhanced quantum coherence between states $|3\rangle$ and $|4\rangle$, reaching a peak of 61.46% at $\Omega_d = 1.6\,\Gamma$. Beyond this optimum, a further increase in the dressing field strength leads to a decrease in C. This reduction is attributed to the excessive AT splitting of the intermediate state $|3\rangle$ induced by the strong dressing field, which makes the dressed states deviate from resonance and degrades interferometric visibility. Figure 3(b) shows the transmitted intensity versus $\delta\phi$ for different Ω_c. The coupling Rabi frequency Ω_c is varied from 1.5 Γ to 5 Γ. In this process, the contrast ratio C increases with Ω_c until it reaches a maximum of 61.46% at $\Omega_c = 4\,\Gamma$, after which it decreases with further increases in Ω_c. To comprehensively illustrate the concurrent influence of both fields, Fig. 4 maps the contrast ratio across the entire 2D parameter space of Ω_d and Ω_c. The 3D surface reveals a distinct maximum, demonstrating that excessive values of either field lead to a noticeable roll-off in visibility. These results confirm that the optimal Rabi frequency configuration is $\Omega_d = 1.6\,\Gamma$ and $\Omega_c = 4\,\Gamma$ under the given conditions.

The fractional phase measurement uncertainty $\delta\phi_{unc}$ is derived based on the error propagation principle ($\delta\phi = \delta I_{noise}/|\partial I/\partial(\Delta\varphi)|$). The system is assumed to operate in the photon shot-noise-limited regime, where the noise standard deviation scales with the square root of the average intensity, i.e., $\delta I_{noise} \approx \sqrt{I_0} = \sqrt{(I_{max} + I_{min})/2}$. Based on Eq. (7), the maximum derivative of the intensity with respect to the phase occurs at the quadrature points, where it takes the exact value of the modulation amplitude B ($|\partial I/\partial(\Delta\varphi)|_{max} = B$). Thus,

$\delta\phi_{\rm unc}$ is given by

$$\delta\phi_{\rm unc} = \frac{\sqrt{I_0}}{B} = \frac{\sqrt{(I_{\rm max}+I_{\rm min})/2}}{|\partial I/\partial(\Delta\varphi)|_{\rm max}}. \tag{9}$$

To validate the rigor of this metric, we evaluate the Fisher information (FI) of the system, defined as $\mathcal{F} \propto (\partial I/\partial\Delta\varphi)^2/\delta I^2_{\rm noise}$. At the optimal quadrature point, the FI reaches its maximum value of $\mathcal{F}_{\rm max} \approx B^2/I_0$, where B denotes the modulation amplitude. Notably, this reveals that Eq. (9) is mathematically equivalent to the Cramér-Rao bound (CRB, $\delta\phi_{\rm CRB} \geq 1/\sqrt{\mathcal{F}_{\rm max}}$). This equivalence indicates that our derived uncertainty represents the fundamental theoretical limit of phase resolution for the proposed atomic homodyne detection scheme. Figures 5 and 6 demonstrate the dual role of the probe field detuning $\Delta_{\rm p}$ in fractional phase measurement. As a critical parameter, it tunes both the contrast ratio C and $\delta\phi_{\rm unc}$ within an optimal range, while excessive values can trigger a half-cycle slip, thereby increasing the measurement uncertainty. Figure 5 shows the influence of $\Delta_{\rm p}$ on the contrast ratio (black dashed line) and the fractional phase measurement uncertainty $\delta\phi_{\rm unc}$. The contrast ratio can be enhanced by tuning the probe field detuning $\Delta_{\rm p}$ between 0 and 3.0 MHz, as evidenced by the numerical results plotted as the black dashed line. Notably, the measurement uncertainty of the fractional phase is reduced simultaneously. The numerical results demonstrate that a high contrast ratio (69.79%–67.15%) and low measurement uncertainty (0.335 rad–0.304 rad) are achieved within a detuning range of 1.7 MHz to 2.5 MHz. The optimal value of $\delta\phi_{\rm unc}$ reaches 0.302 rad at $\Delta_{\rm p} = 2.6$ MHz, which corresponds to a high-precision measurement at the sub-radian level. By balancing both the high contrast ratio and the low measurement uncertainty, the optimal probe field detuning is determined to be 2.5 MHz.

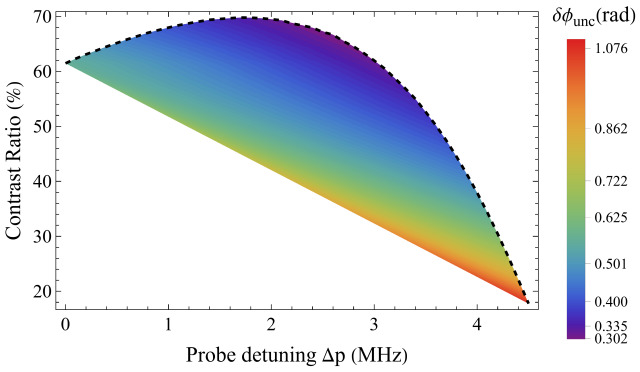


Fig. 5. Relationship between the probe field detuning $\Delta_{\rm p}$, contrast ratio C, and $\delta\phi_{\rm unc}$. Other parameters are the same as those in Fig. 2.

A half-cycle slip is a critical problem in carrier phase observations, requiring detection and correction for reliable navigation and metrology solutions. It is characterized by an abrupt phase shift of half a cycle (i.e., 0.5 cycles, where one cycle is 2π). As shown in Fig. 6(a), this occurs when the probe field detuning $\Delta_{\rm p} \geq 3.3$ MHz. The magnitude of the half-cycle slip increases with the probe field detuning over the range of 3.3 to 4.5 MHz. This occurs because excessive detuning of the probe field reduces the coherence of the $|1\rangle \rightarrow |2\rangle$ transition, which in turn disrupts the initial population and ultimately breaks the deterministic mapping between the fractional phase $\delta\phi$ and the transmitted intensity I. This effect manifests as significant fluctuations in the dispersion curve, leading to discontinuous phase accumulation in the form of π-phase jumps and a reduction in the modulation amplitude of the transmitted intensity. The evolution of the phase dispersion curve with probe field detuning is presented in Fig. 6(b). Below the optimum of 2.5 MHz, the curve shows only mild fluctuations. Beyond a threshold of $\Delta_{\rm p} = 3.3$ MHz, it transitions to a regime of drastic fluctuations, where the amplitude intensifies and the half-cycle slip becomes increasingly pronounced. Concurrently, the contrast ratio drops significantly from 67.15% to 17.75%. This degradation limits the achievable resolution of the fractional phase measurements, as demonstrated by the corresponding numerical results in Fig. 5.

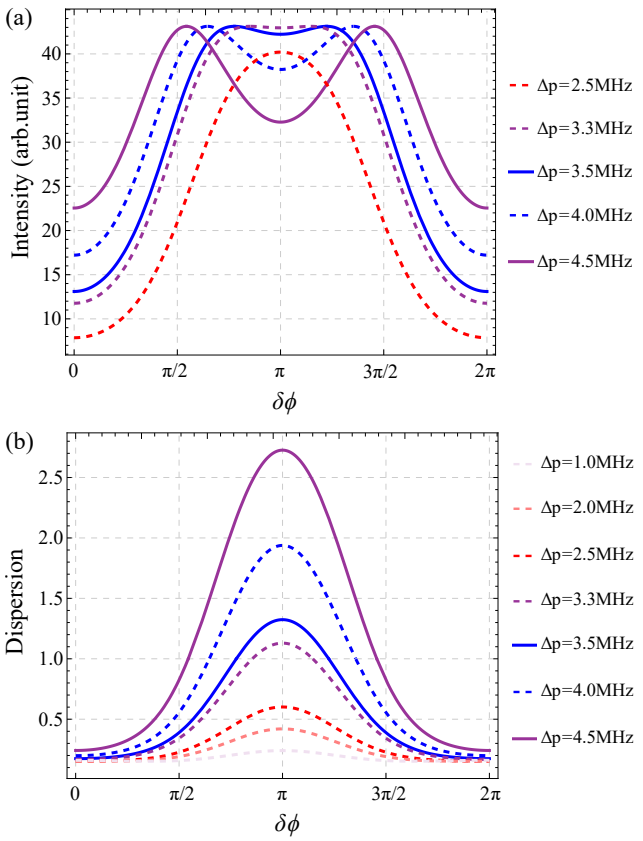


Fig. 6. (a) Half-cycle slip of the fractional phase in the transmitted intensity profile. (b) Variation in the degree of dispersion of the fractional phase $\delta\phi$ with the probe field detuning $\Delta_{\rm p}$. ($E_{\rm B1C} = 0.2$ V/m, $E_{\rm LO} = 2$ V/m. Other parameters are the same as those in Fig. 2.)

Having identified the optimal configuration ($\Omega_{\rm c} = 4\,\Gamma$, $\Omega_{\rm d} = 1.6\,\Gamma$, and $\Delta_{\rm p} = 2.5$ MHz) for the Rydberg atom antenna, we next analyze the effect of the BDS-3 B1C signal strength $E_{\rm B1C}$ on carrier-phase observations. Figure 7(a) presents the transmitted intensity of the fractional phase for

E_{B1C} ranging from 0.01 to 0.25 V/m. The contrast ratio increases monotonically with E_{B1C}, reaching a maximum value of 74.79% at $E_{\mathrm{B1C}} = 0.25$ V/m. The influence of E_{B1C} on the fractional phase measurement uncertainty is shown in Fig. 7(b). As E_{B1C} increases from 0.048 to 0.1 V/m, $\delta\phi_{\mathrm{unc}}$ varies between 1.0 and 0.5 rad, maintaining a basic sub-radian level. When E_{B1C} further increases to the range of 0.11–0.25 V/m, $\delta\phi_{\mathrm{unc}}$ decreases from 0.4635 to 0.2730 rad, achieving a high-precision sub-radian level. A linear fit to the data on a log–log scale yields the power-law relationship $\delta\phi_{\mathrm{unc}} \approx 0.055 \times E_{\mathrm{B1C}}^{-0.962}$, as shown by the black dashed line in Fig. 7(b). The scaling exponent $s \approx -0.962$ is close to -1, indicating that $\delta\phi_{\mathrm{unc}}$ is approximately inversely proportional to E_{B1C}. The sensitivity of this relationship is quantified by the prefactor $k \approx 0.055$. A smaller k corresponds to higher resolution in fractional phase measurements when the BDS-3 B1C signal strength remains unchanged.

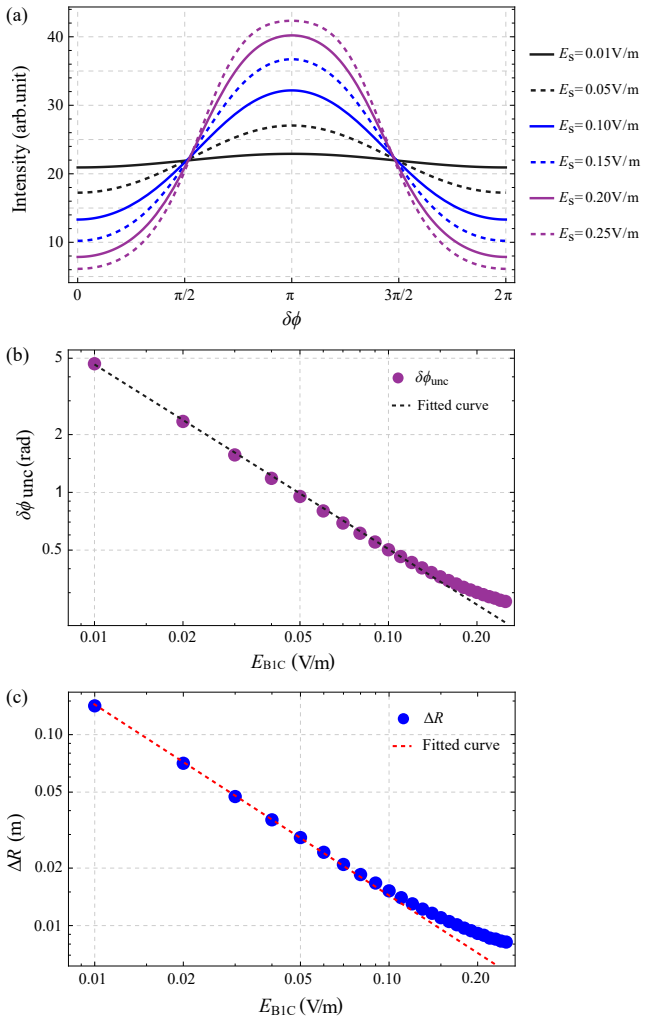


Fig. 7. (a) Fractional phase for E_{B1C} (E_{s}) in the range of 0.01 V/m to 0.25 V/m. $E_{\mathrm{LO}} = 2$ V/m. (b) Power-law fitting between E_{B1C} and $\delta\phi_{\mathrm{unc}}$ in log–log coordinates. (c) Inverse fitting between E_{B1C} and ΔR in log–log coordinates. Other parameters are the same as those in Fig. 2.

The distance measurement error ΔR is derived from the wavelength λ and the fractional phase measurement uncertainty $\delta\phi_{\mathrm{unc}}$ as

$$\Delta R = \frac{\lambda}{2\pi} \cdot \delta\phi_{\mathrm{unc}}, \tag{10}$$

where $\lambda \approx 0.19$ m. Thus, variations in E_{B1C} affect the distance measurement error, as shown in Fig. 7(c). The numerical results show that the distance measurement error $\Delta R < 1$ cm when $E_{\mathrm{B1C}} > 0.15$ V/m. This means that increasing E_{B1C} can reduce distance measurement errors in fractional phase measurements. By applying a logarithmic transformation to the data and performing linear fitting in double-logarithmic coordinates, it is found that the distance measurement error ΔR is inversely proportional to the signal amplitude E_{B1C}, i.e., $\Delta R = 0.0014/E_{\mathrm{B1C}}$. This indicates that $\Delta R \propto 1/E_{\mathrm{B1C}}$. The fitting parameter $a = 0.0014$ V acts as the proportionality coefficient for the distance measurement error ΔR, where a smaller value of a indicates better measurement performance. This relationship can be used to estimate the distance measurement error.

4. Conclusion

In conclusion, we propose a scheme for carrier phase observation of the BDS-3 B1C signal using Rydberg atoms. The introduction of an auxiliary microwave dressing field prepares Rydberg states with higher angular momentum $L = 3$, enabling detection of the BDS-3 B1C signal while narrowing the EIT linewidth, thereby facilitating high-precision measurement of the signal's fractional phase. The numerical results demonstrate that our approach reduces the fractional phase measurement uncertainty to the sub-radian level, with minimum distance measurement errors below 1 cm. Furthermore, we elucidate the physical mechanism of the half-cycle slip and its impact on observation uncertainty. This scheme holds potential for satellite communication, quantum radar positioning, and next-generation navigation systems such as NTS-3. At the current stage, this study primarily serves as a theoretical exploration at the physical level, focusing on validating the fundamental physical feasibility of the single-frequency carrier mechanism under idealized conditions. To fully evaluate its practical feasibility, future system-level studies will address critical engineering constraints, such as high-dynamic Doppler shifts, multipath effects, and signal-to-noise ratio (SNR) requirements.

Acknowledgments

Project supported by the Natural Science Foundation of Shandong Province, China (Grant Nos. ZR2025MS67 and ZR2021LLZ006), the National Innovation and Entrepreneurship Training Program for College Students, China (Grant No. 202410424062), and the Research Project on Postgrad-

uate Education and Teaching Reform of Shandong Province, China (Grant Nos. SDYJSJGC2024016 and Yzlts2024016).

References

[1] Chen Q, Chen H, Jiang W, Zhou X and Yuan P 2018 *J. Navig.* **71** 1492
[2] Zhao D, Roberts G W, Hancock C M, Lau L and Bai R 2019 *GPS Solut.* **23** 22
[3] Guoping H and Lingjuan M 2012 *Chin. J. Aeronaut.* **25** 227
[4] Havyarimana V, Xiao Z, Bizimana P C, Hanyurwimfura D and Jiang H 2020 *IEEE Trans. Instrum. Meas.* **70** 1
[5] He Y, Han M, Li Q, Jia Z, Chen B, Wang L, Parniak M and Peng Y 2023 *Opt. Commun.* **545** 129639
[6] Cao Y, Zhang H, Zhang L, Xiao L and Jia S 2025 *Opt. Express* **33** 7753
[7] Anderson D A, Sapiro R E and Raithel G 2020 *IEEE Aerosp. Electron. Syst. Mag.* **35** 48
[8] Zhu G L, Hu C S, Wang H, Qin W, Lü X Y and Nori F 2024 *Phys. Rev. Lett.* **132** 193602
[9] Bin Q, Wu Y, Gao J H, Chen A, Nori F and Lü X Y 2025 *Phys. Rev. Lett.* **135** 103602
[10] You S, Cai M, Zhang H, Xu Z and Liu H 2023 *Photonics* **10** 328
[11] Ge S, Ren G, Wang W, You Y, Jia Z, Chen B, van den Brink A M and Peng Y 2024 *Opt. Express* **32** 22615
[12] Elgee P K, Hill J C, LeBlanc K J E, Ko G D, Kunz P D, Meyer D H and Cox K C 2023 *Appl. Phys. Lett.* **123** 084001
[13] Sedlacek J A, Schwettmann A, Kübler H, Löw R, Pfau T and Shaffer J P 2012 *Nat. Phys.* **8** 819
[14] Zhou F, Qi Y, Sun H, Chen D, Yang J, Niu Y and Gong S 2013 *Opt. Express* **21** 12249
[15] Xu X Y, Xie G, Ma J, Ying L, Yuan J, Huang Z and Sha W E 2024 *Opt. Express* **32** 21755
[16] Jing M, Hu Y, Ma J, Zhang H, Zhang L, Xiao L and Jia S 2020 *Nat. Phys.* **16** 911
[17] Borówka S, Pylypenko U, Mazelanik M and Parniak M 2024 *Nat. Photonics* **18** 32
[18] Jau Y Y and Carter T 2020 *Phys. Rev. Appl.* **13** 054034
[19] Anderson D A, Sapiro R E and Raithel G 2020 *IEEE Trans. Antennas Propag.* **69** 2455
[20] Anderson D A, Paradis E, Raithel G, Sapiro R E and Holloway C L 2018 *2018 11th Global Symposium on Millimeter Waves (GSMM) (IEEE)* pp. 1–3
[21] Hu J, Li H, Song R, Bai J, Jiao Y, Zhao J and Jia S 2022 *Appl. Phys. Lett.* **121** 014002
[22] Rotunno A P, Berweger S, Prajapati N, Simons M T, Artusio-Glimpse A B, Holloway C L, Jayaseelan M, Potvliege R M and Adams C S 2023 *J. Appl. Phys.* **134** 144001
[23] Holloway C L, Gordon J A, Jefferts S, Schwarzkopf A, Anderson D A, Miller S A, Thaicharoen N and Raithel G 2014 *IEEE Trans. Antennas Propag.* **62** 6169
[24] Chu L J 1948 *J. Appl. Phys.* **19** 1163
[25] Cox K C, Meyer D H, Fatemi F K and Kunz P D 2018 *Phys. Rev. Lett.* **121** 110502
[26] Yang K, Mao R, An Q, Li J, Sun Z and Fu Y 2023 *Sens. Actuators A Phys.* **351** 114167
[27] Holloway C L, Simons M T, Gordon J A and Novotny D 2019 *IEEE Antennas Wirel. Propag. Lett.* **18** 1853
[28] Liu Z K, Zhang L H, Liu B, Zhang Z Y, Guo G C, Ding D S and Shi B S 2022 *Nat. Commun.* **13** 1997
[29] Schmidt M, Bohaichuk S, Venu V, Christaller F, Liu C, Ripka F, Kübler H and Shaffer J P 2024 *Opt. Express* **32** 27768
[30] Pan R K, Tang L and Xia K 2024 *Phys. Rev. A* **110** 043505
[31] Yang W, Jing M, Zhang H, Zhang L, Xiao L and Jia S 2024 *Opt. Lett.* **49** 2938
[32] Anderson D, Sapiro R, Gonçalves L, Cardman R and Raithel G 2022 *Phys. Rev. Appl.* **17** 044020
[33] Berweger S, Artusio-Glimpse A B, Rotunno A P, Prajapati N, Christesen J D, Moore K R, Simons M T and Holloway C L 2023 *Phys. Rev. Appl.* **20** 054009
[34] Han Y, He C, Xu P, Zhao Y, Wang T and Li W 2025 arXiv:2501.10989 [quant-ph]
[35] Song D, Jiao Y, Hu J, Yin Y, Li Z, He Y, Bai J, Zhao J and Jia S 2024 *Appl. Phys. Lett.* **125** 194001
[36] Liu X B, Jia F D, Zhang H Y, *et al.* 2022 *Chin. Phys. B* **31** 090703
[37] Brown R C, Kayim B, Viray M A, Perry A R, Sawyer B C and Wyllie R 2023 *Phys. Rev. A* **107** 052605
[38] Fan H, Kumar S, Sedlacek J, Kübler H, Karimkashi S and Shaffer J P 2015 *J. Phys. B: At. Mol. Opt. Phys.* **48** 202001
[39] Liu Y Q, Zhang J N, Wang Y X, Mei J, Jia F D, Gao K Y, Zhu W W and Zhong Z P 2026 *Opt. Express* **34** 651
[40] You S, Cai M, Zhang S, Xu Z and Liu H 2022 *Opt. Express* **30** 16619
[41] Wu S, Ni R, Gong C, Zhu Q, Jiang G and Yang G 2024 *2024 IEEE INC-USNC-URSI Radio Science Meeting (Joint with AP-S Symposium)* pp. 193–194
[42] Steck D A 2001 *Rubidium 85 D Line Data*
[43] Sibalić N, Pritchard J D, Adams C S and Weatherill K J 2017 *Comput. Phys. Commun.* **220** 319
[44] Meyer D H, Kunz P D and Cox K C 2021 *Phys. Rev. Appl.* **15** 014053